NANOSCALE MULTIMODAL ANALYSIS OF SENSITIVE NANOMATERIALS BY MONOCHROMATED STEM-EELS IN LOW-DOSE AND CRYOGENIC CONDITIONS

Maeva Chaupard, Jéril Degrouard, Xiaoyan Li, Odile Stéphan, Mathieu Kociak, Ruxandra Gref, Marta de Frutos

NANOSCALE MULTIMODAL ANALYSIS OF SENSITIVE NANOMATERIALS BY MONOCHROMATED STEM-EELS IN LOW-DOSE AND CRYOGENIC CONDITIONS

*Maeva Chaupard,[a,b] Jéril Degrouard,[a] Xiaoyan Li,[a] Odile Stéphan,[a] Mathieu Kociak,[a] Ruxandra Gref,[b] Marta de Frutos[a]**

[a]Laboratoire de Physique des Solides, CNRS, UMR 8502, Université Paris-Saclay, F-91405 Orsay, France

[b]Institut des Sciences Moléculaires d'Orsay, CNRS, UMR 8214, Université Paris-Saclay, F-91405 Orsay, France

**Marta de Frutos

Email: marta.de-frutos@universite-paris-saclay.fr

ABSTRACT

Scanning Transmission Electron Microscopy coupled with Electron Energy Loss Spectroscopy (STEM-EELS) provides spatially resolved chemical information down to the atomic scale. However, studying radiation-sensitive specimens such as organic-inorganic composites remains extremely challenging. Here, we analysed metal-organic framework nanoparticles (nanoMOFs) at low-dose (10 $\bar{e}/Å^2$) and liquid nitrogen temperatures similar to cryo-TEM conditions, usually employed for high-resolution imaging of biological specimens. Our results demonstrate that monochromated STEM-EELS enables damage-free analysis of nanoMOFs, providing in a single experiment, signatures of intact functional groups comparable with infrared, ultraviolet and X-ray data, with an energy spectral resolution down to 7 meV. The signals have been mapped at the nanoscale (< 10 nm) for each of these energy spectral ranges, including the chemical features observed for high energy losses (X-ray range). By controlling beam irradiation and monitoring spectral changes, our work provides insights into the possible pathways of chemical reactions occurring under electron exposure. These results demonstrate the possibilities for characterising at the nanoscale the chemistry of sensitive systems such as organic and biological materials.

Keywords: Radiation-sensitive nanomaterials, multimodal analysis, monochromated STEM-EELS, low-dose analysis, high-resolution spectromicroscopy, organic-inorganic nanoparticles, metal-organic frameworks.

Nanosized metal-organic frameworks (nanoMOFs) are organic-inorganic nanomaterials with a three-dimensional structure created by the self-assembly of organic linkers and metal clusters. With their versatile compositions and high porosity, nanoMOFs are of great interest for gas storage,[1] wastewater treatment,[2] catalysis,[3] sensing[4] and drug delivery.[5] Providing comprehensive and reliable characterisation of such materials is a significant step in the development of applications but remains challenging due to their nanometric sizes together with their complex structures and compositions. In this regard, spectromicroscopies have been developed, constantly pushing the limits of spatial and energy resolutions. These analytical techniques exploit photons, ions or electrons interactions[6] to explore nanomaterial local physical and chemical properties. Among them, Scanning Transmission Electron Microscopy coupled with Electron Energy Loss Spectroscopy (STEM-EELS) offers the possibility of a deep chemical analysis down to the atomic scale.[7] In this approach, hyperspectral data are acquired by a point-by-point rastering of the electron probe over the area of interest, providing simultaneously imaging and local information on the electronic and vibrational transitions induced by the interaction of the incident electrons with the specimen. The last generation microscopes equipped with monochromated electron guns cover excitations over a wide energy range from tens of meV (far infrared -IR- range) to hundreds of eV (soft X-rays) with an energy resolution (δE) reaching $\lesssim$ 10 meV.[7]

However, studying organic and organic-inorganic nanomaterials remains a delicate task, as they are extremely sensitive to radiation damage. Beam-induced-radiolysis and knock-on may result in structural (shrinking, amorphisation) and chemical damages (loss of mass and bond breakage), affecting the nanomaterial's integrity.[8–10] Noticeably, by employing damage preventive conditions (cryo-holder, low-dose or aloof configuration), recent papers have shown the powerful possibilities offered by EELS for deep characterisation of organic molecules, polymers, MOFs and MOF glass composites in the energy ranges corresponding to IR,[11–14]

UV[15–17] and X-rays.[10,18] But to date, none of them has coupled the analysis in the three energy windows. Yet, exploiting the entire energy range would provide a signal complementarity allowing an in-depth characterisation of the nanomaterial composition but also monitoring reactional mechanisms.

With the aim of using the full potential of STEM-EELS, we report in the following a nanoscale multimodal spectroscopic analysis of nanoMOFs. Among their large family, we selected MIL-100(Fe), MIL-100(Al) and UiO-66 nanoparticles, where MIL and UiO stand for Material of Institute Lavoisier and Universitetet i Oslo, respectively. MIL-100 are self-assembled from benzene tricarboxylic acid (BTC) and iron or aluminium ions, while UiO-66 consist of the coordination of zirconium ions with benzene dicarboxylic acid (BDC). For the three of them, the metal-linker coordination bond involves carboxylate functions. As previously reviewed by Liu *et al.*,[19] MOFs are generally highly sensitive to the electron beam. The authors indicated a beam tolerance dose ranging from 5 $\bar{e}/Å^2$ to 30 $\bar{e}/Å^2$ for several widely studied MOFs (MIL-101, MOF-5, NU-1000, UiO-66 and ZIF-8 where NU and ZIF stand for Northwestern University and Zeolitic Imidazolate Framework), by monitoring the diffraction spot fading with exposure. Others have also demonstrated the structural and molecular modification of ZIF-L by monitoring the diffraction spot fading and EELS signatures above tens of $\bar{e}/Å^2$.[10] Although few in number, these studies suggest that MOF materials exhibit a different beam tolerance dose depending on their nature. Because of the extreme radiation sensitivity of MIL-100(Fe) and UiO-66, high-resolution STEM imaging was only possible with low-dose conditions, of the order of 10 $\bar{e}/Å^2$.[20,21] On the opposite, to the best of our knowledge, MIL-100(Al) have not been studied yet by STEM. At last, none of the three nanoMOFs has been carefully characterised by EELS. The main reason for the lack of damage-free EELS analysis is the difficulty of getting a measurable signal at low doses. Therefore, many questions still need unravelling for a better understanding of these nanoMOFs properties.

Here, we present intact nanoMOFs data obtained from monochromated STEM-EELS measurements at cryogenic temperatures and low-dose (10 $\bar{e}/Å^2$), by using a direct detection camera allowing the detection of very weak signals.[22] By exploring the three energy ranges (corresponding to IR, UV and X-ray intervals), we provide a comprehensive study of the nanoMOFs' chemical signatures with an energy resolution down to 7 meV. First, we investigate the local chemical reactions occurring under controlled beam irradiation with a systematic approach revealing complex mechanisms. Then, we demonstrate the possibility of characterising intact nanoMOFs at low-dose. Each feature was compared with infrared, ultraviolet and X-ray data to be assigned to specific functional groups. Finally, by extracting the corresponding spectral features, we map the nanoMOFs' signature over the three energy ranges with a nanoscale spatial resolution. By exploiting the whole EELS energy range, our results provide damage-free analysis of these sensitive specimens and offer a better understanding of their complex nanostructures.

RESULTS AND DISCUSSION

NanoMOFs crystal structure

We performed cryo-transmission electron microscopy (cryo-TEM) imaging of the three nanoMOFs. This technique has the advantage of assessing the crystallinity of the specimens on a single-particle basis. As shown in **Figure 1a-c**, the nanoparticles display well-faceted morphologies typical of MIL-100(Al),[23] MIL-100(Fe)[24] and UiO-66.[25] Their sizes range from 40 nm to 300 nm for MIL-100, and from 100 nm to 1.2 µm for UiO-66. The images show the crystal structures with a spatial resolution of 6 Å along the [112], [110] and [532] directions for MIL-100(Al), MIL-100(Fe), and UiO-66, respectively. These results are in good agreement with previous studies, showing the cubic structure (Fd-3m space group) of MIL-100[20] and UiO-66.[21] However, the observation of the UiO-66 structure, which has previously revealed details

below 2 Å,[21] was partially hampered here by the TEM spatial resolution. Because the present cryo-TEM images were obtained in low-dose conditions (total dose estimated between 10 and 15 $\bar{e}/Å^2$) no structural damage was observed for a single image acquisition. However, due to the extreme radiation sensitivity of the nanoMOFs, the high-resolution information tended to disappear after consecutive image acquisitions over the same area. The observed loss of crystallinity in TEM gives a rough estimation of the beam tolerance dose of these nanoMOFs. Hence, similar low-doses have been applied in STEM acquisitions for a damage-free analysis of the specimens.

Figure 1d provides a schematic representation of the nanoMOF chemical structures. Since the three specimens exhibit different structures, it depicts a simplified model composed of the metal (labelled M) coordinated to the linkers but does not describe the minor specificities of each system. To help the reading, the chemical bonds described in this manuscript are indicated. We will refer to this schema throughout the manuscript.

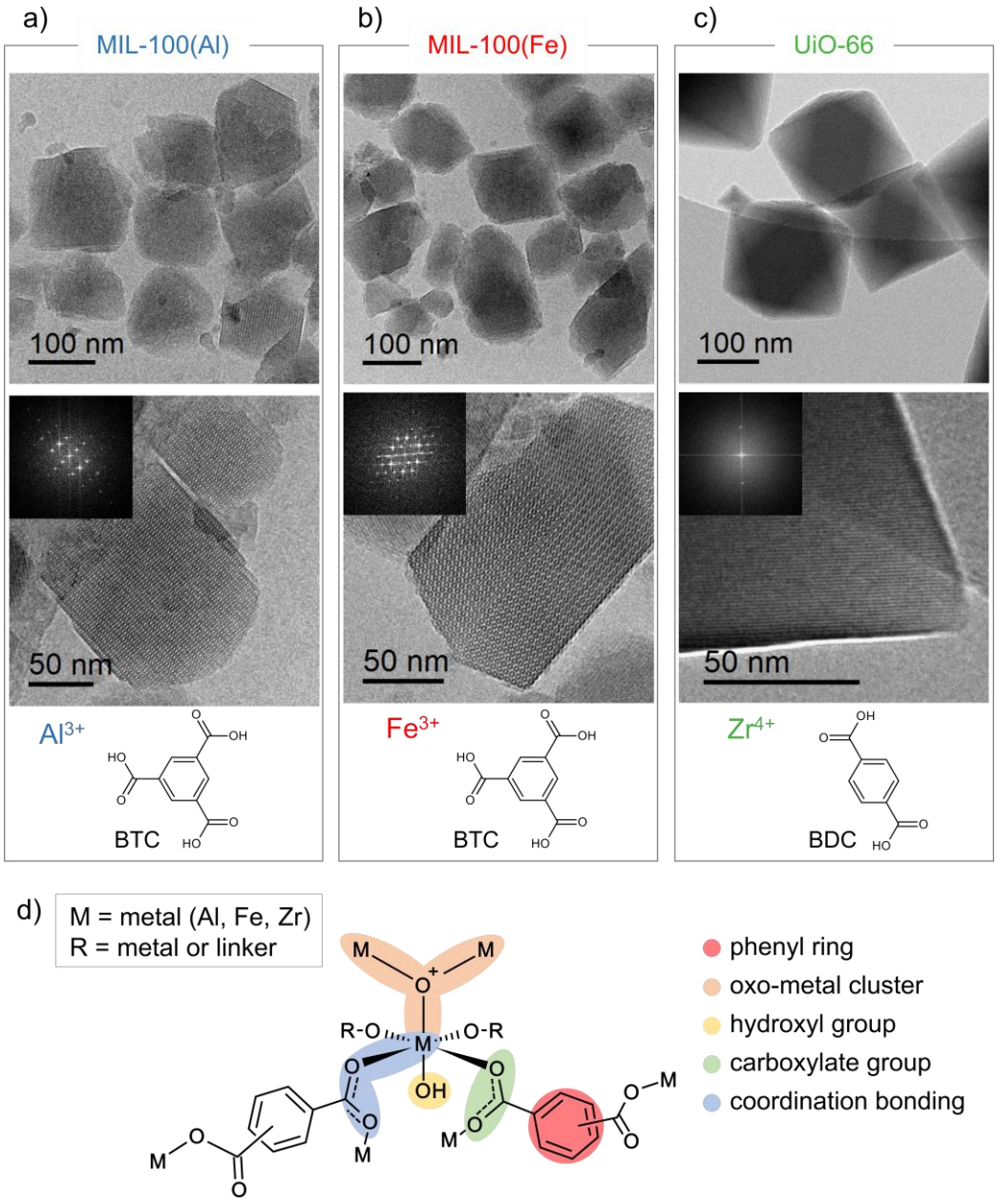

Figure 1. *Cryo-TEM images of (a) MIL-100(Al), (b) MIL-100(Fe), and (c) UiO-66 nanoparticles. The top row images illustrate their well-faceted morphologies. At higher magnification, the middle row images show their crystal planes with a spatial resolution of 6 Å along the (a) [112], (b) [110] and (c) [532] directions, respectively. The corresponding fast Fourier transforms are shown on the inset. The chemical components of each nanoMOFs are indicated in the bottom row. (d) Schematic representation of the molecular structure of the three nanoMOFs. For simplicity, the different MIL-100 and UiO-66 structures have been generalised using atom labelling (M for metals and R for metals or linkers). OH groups represent hydroxyl groups found in the three nanoMOFs or MIL-100 structural water. The colours relate the chemical groups to their designation employed in the main text.*

EELS: a multimodal analysis for radiation-sensitive material

STEM-EELS was used for an in-depth analysis of the three nanoMOFs. **Figure 2a** shows a schematic representation of the microscope setup. The focused electron beam is scanned over the area of interest (typically 400 x 400 nm^2) giving hyperspectral data (the so-called Spectrum Imaging mode[26]). At each beam position, an image of the specimen is acquired on the High Angle Annular Dark Field (HAADF) detector and simultaneously, the EEL spectrometer measures the energy lost by the electrons, providing spatially resolved chemical information. In the present work, we used a highly monochromated Nion Hermes 200-S microscope fitted with a Nion Iris spectrometer and a Quantum Detectors Merlin direct electron detector. This combination provides ultimate energy resolution ($\delta E \lesssim 10$ meV) and high energy range (from far IR to soft X-rays) together with a high sensitivity that is crucial for dose-limited measurements (see Experimental section). As shown in **Figure 2b**, EELS data cover a wide energy range: the ultralow-loss (ULL) region (below 2 eV, < 16000 cm^{-1}) associated with vibrational excitations down to the far IR; the low-loss (LL) region involving valence excitations from the visible to the vacuum UV energy range (2 – 50 eV, equivalent to 25 – 620 nm); and the core-loss (CL) region (above 50 eV) that, similarly to soft X-ray absorption spectroscopies, reveals the electronic structure of the material through the analysis of their atomic ionisation edges. With a wide energy window spanning 400 eV, we collected simultaneously the LL and CL signals (energy resolution $\delta E = 800$ meV). A closer look at the individual LL and CL features was achieved with a higher energy resolution ($\delta E = 40$ meV for 16 eV energy window or $\delta E = 220$ meV for 116 eV energy window). Because the ULL features are located at very small energy losses (hundreds of meV), they appear as weak signals superimposed on the intense zero-loss peak (ZLP), corresponding to unscattered electrons transmitted with no energy loss through the specimen. Hence, ULL analysis requires an even higher energy resolution corresponding to a narrower energy window (1.6 eV energy window,

δE = 12 meV). For each energy window, the energy resolution δE was measured on the EELS detector from the full-width at half-maximum of the ZLP (see SI for an extensive discussion of the energy resolution and its dependence with acquisition and detection conditions). It should be highlighted that our observations were only possible thanks to the use of a direct detection camera whose high sensitivity and very low noise improve the signal-to-noise ratio (SNR) and whose high dynamic range allows the simultaneous collection of the huge ZLP along with the weak CL signal with no saturation nor loss of sensitivity.[22]

As nanoMOFs are extremely sensitive to the electron beam, their analysis requires special care to prevent degradation under electron irradiation. Therefore, the study was carried out by using i) a cryo-specimen holder cooled down to 125 K; ii) a 10 mrad convergence semi-angle enabling sub-nanometer beam sizes (far from the ultimate microscope performance) to decrease the electron current density; and iii) low electron dose conditions (see details in SI). By adjusting the probe current, the acquisition time and image pixel size, we reached total doses down to 10 $\bar{e}/Å^2$, as low as those employed for cryo-TEM imaging of biological specimens.[27] Then, the beam-induced damage effect was studied by increasing the dose up to 10^4 $\bar{e}/Å^2$ (details on total dose and dose rate calculations are given in SI). To do so, data were collected either by a single acquisition on different areas or several successive acquisitions on the same area. In the following, the corresponding total doses are named *single acquisition dose* or *cumulative dose*, respectively (more details in SI). At least six hyperspectral images were acquired for each electron dose condition on different nanoparticles to provide statistical analysis. Note that, to adjust the electron dose, the study was performed with relatively large pixel sizes, restraining the spatial resolution: the lowest electron dose was obtained with a pixel of 10 nm while higher doses were reached for pixels of 1 nm.

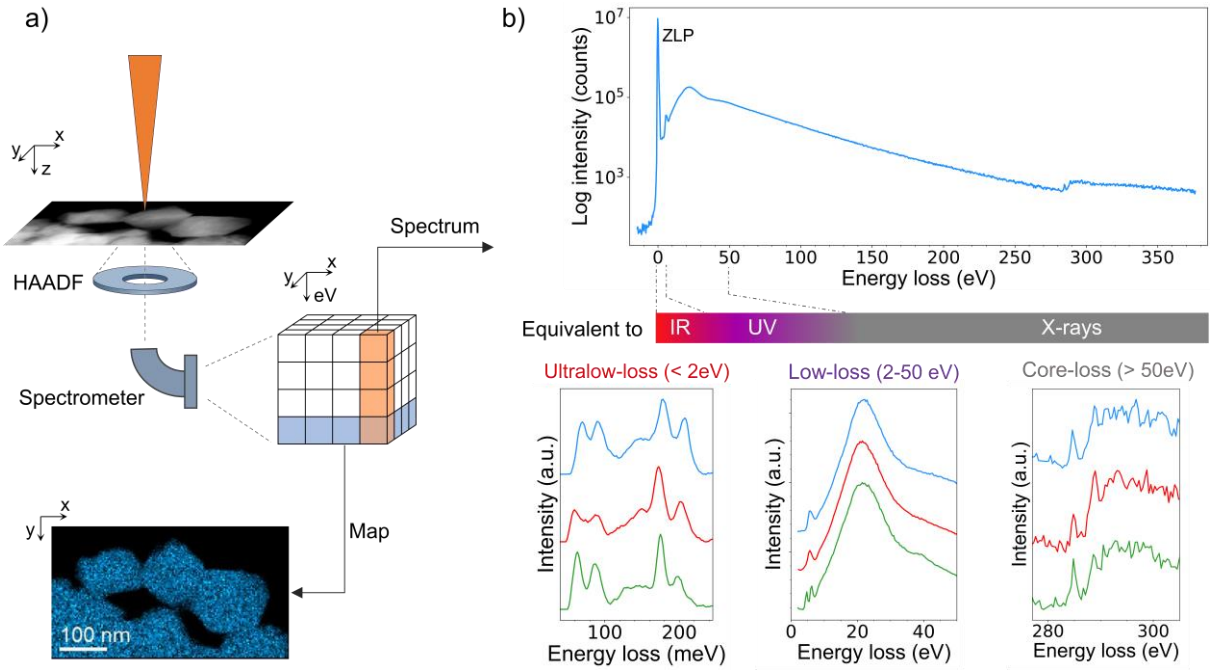

***Figure 2**. Schematic representation of STEM-EELS. (a) The scanning electron probe acquires hyperspectral images with a nanoscale spatial resolution. It offers a multimodal analysis ranging from the vibrational to the soft X-ray energy window. (b) At the top, the widest energy window (spanning 400 eV, δE = 800 meV) enables simultaneously analysing of the LL and CL signals. ULL was not distinguishable at this energy resolution. Here, the signature of MIL-100(Al) is shown at low-dose. At the bottom: enlarged views of the LL (on the middle) and CL signals (on the right) obtained at low-dose for the three nanoMOFs. ULL spectra (on the left) were acquired at 120 ē/Å^2 with a narrower energy window (spanning 1.6 eV, δE = 12 meV). Blue, red and green colours represent the spectra obtained for MIL-100(Al), MIL-100(Fe) and UiO-66, respectively.*

Core-loss excitations

We first analysed the inner electron shell excitations of the nanoMOFs on the carbon and oxygen K-edges (**Figures 3a and 3c**). The two spectra show changes in the chemical signatures as a function of the electron dose. The carbon K-edge evolution of MIL-100(Al) is presented in **Figure 3a** (blue lines). Similar evolutions are observed for MIL-100(Fe) and UiO-66 in Figure S1. All spectra were calibrated by setting the ZLP at 0 eV and the characteristic peak of amorphous carbon (grey line in **Figure 3a**) at 285.0 eV.[28] In **Figure 3a**, the spectrum of MIL-100(Al) obtained at low-dose (10 ē/Å^2), reveals two intense peaks, at 285.0 eV (denoted CL_1) and 288.7 eV (denoted CL_3), and a weak signal at 291.1 eV (denoted CL_4). EELS CL spectra are directly comparable to the corresponding X-ray absorption data obtained in the same energy

range.[29,30] Nonetheless, the carbon K-edge of these nanoMOFs has never been studied with such techniques. Hence, we compare our EELS results with the Near-Edge X-ray Absorption Fine Structure (NEXAFS) spectra of the free-standing organic linkers (black line in **Figure 3a**, grey line in Figure S2). As shown in **Figure 3a**, CL_1, CL_3 and CL_4 features of MIL-100(Al) are compatible with those previously reported for BTC by NEXAFS.[31] This good agreement demonstrates that low-dose EELS features of nanoMOFs are damage-free signatures. They are respectively related to 1s–$\pi^*_{C=C}$ transitions in phenyl rings (CL_1), 1s–π^*_{COO} transitions in carboxyl groups (CL_3) and 1s–σ^*_{C-C} transitions in phenyl rings (CL_4).[31,32] A similar comparison between low-dose EELS and NEXAFS for MIL-100(Fe), UiO-66, BTC and BDC can be found in Figure S2. The similarities between nanoMOFs entities and their linkers are consistent since the organic part of the nanoparticles is the only contribution to the carbon K-edge, the data having been recorded above vacuum, on the grid carbon holes. Besides, it should be mentioned that the lack of influence from the metal coordination is not surprising since it is achieved through oxygen atoms of carboxyl groups. One could expect additional 1s–σ^*_{C-H} transitions in phenyl rings near 287 eV, as previously demonstrated by NEXAFS and EELS studies on BDC,[32] BTC (see NEXAFS data in Figure S2) and other benzene derivatives.[18,33–35] Here, its absence is probably due to instantaneous dehydrogenation under electron irradiation.[36] Except for beam-induced dehydrogenation, our low-dose EELS results are similar to linkers NEXAFS data, revealing spectral features characteristic of intact functional groups.

When increasing the electron dose, spectral changes illustrate the evolution of the specimen's chemical composition as a result of radiolysis. First, a slight reduction and broadening of peak CL_1 are observed with an enhancement of peak CL_4. The decrease of peak CL_1 reflects the breakage of C=C bonds, while its broadening outlines the formation of new types of chemical bonds induced by irradiation. Upon irradiation, its shape tends to be similar to amorphous carbon (grey line in **Figure 3a**). In the meantime, the peak CL_4 increase is associated with the

formation of C-C bonds, which can be closely related to the radiolysis of benzene double bonds. More significantly, an intense peak (denoted CL_2) rises at 287.6 eV along with a drastic reduction of the peak CL_3. It indicates the formation of a new species and the breakage of the -COO bonds of the carboxyl groups. According to the literature, the peak CL_2 can be attributed to $1s–\pi^*_{C=O}$ transitions of the carbonyl groups (-CO).[33,35] This evolution indicates that, under beam-induced radiolysis, the carboxyl species are presumably converted into carbonyl by the reduction of the organic linkers. For higher electron doses (above 310 $\bar{e}/Å^2$), the same trend continues without further changes illustrating the robustness of the carbonyl (-CO) composite created under irradiation (shown in Figure S1 for electron doses up to 780 $\bar{e}/Å^2$).

By monitoring the chemical evolution under irradiation, our study enables us to relate the features observed at high electron doses (usually employed for the EELS analysis) with the chemical functions of the original intact nanomaterial. For instance, previous EELS studies of biominerals performed above 100 $\bar{e}/Å^2$ have systematically reported a peak at 287 eV, similar to CL_2, as a fingerprint of the organic fraction.[37–40] Here, we show that this feature can correspond to the degraded signature of components containing carboxyl functions, which in the case of biominerals could correspond to fatty acids or proteins.

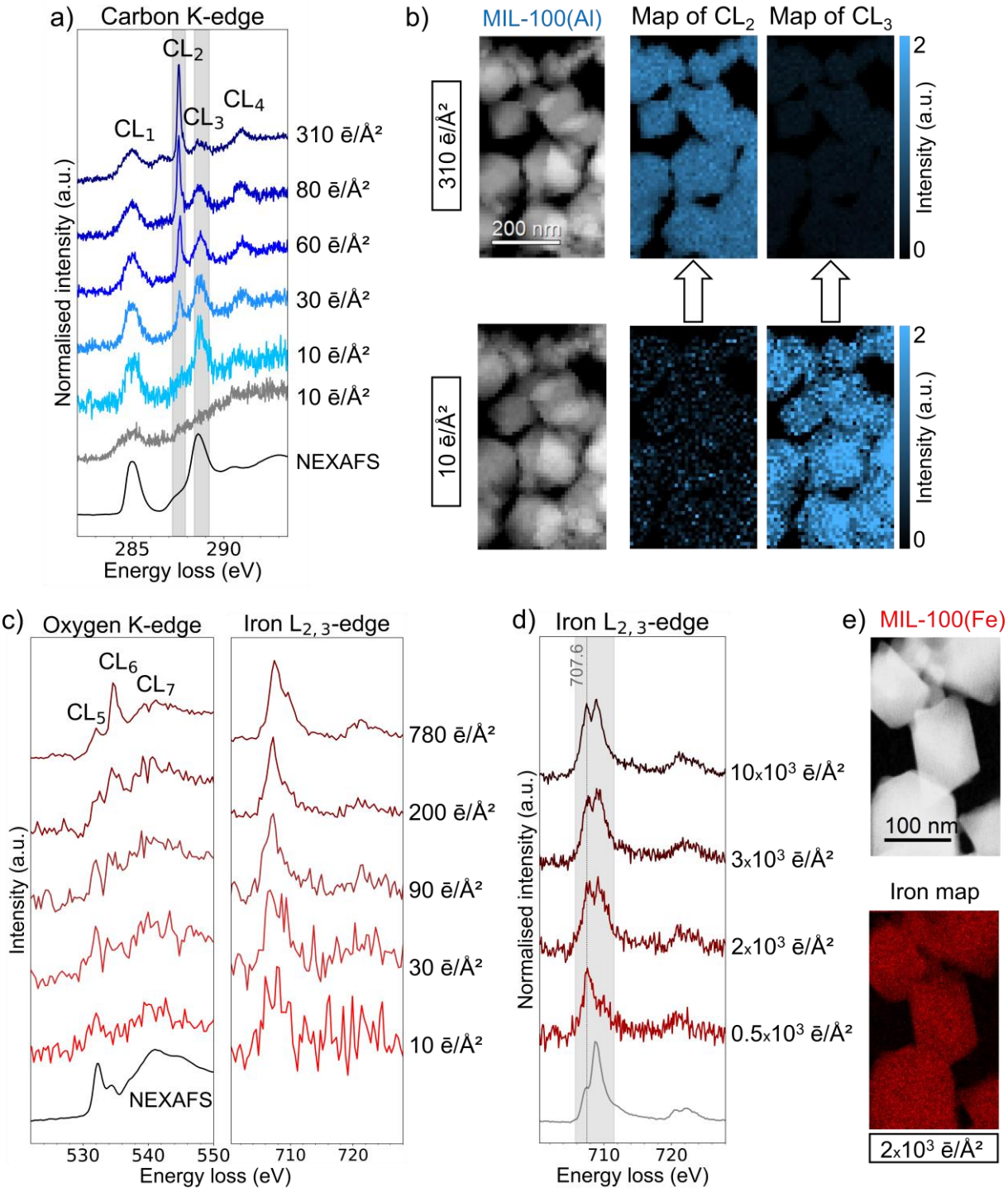

Figure 3. *Core-loss analysis of MIL-100 nanoparticles as a function of the electron dose. All spectra are average features obtained by extracting and summing the signal over the whole hyperspectral image. (a) Evolution of the carbon K-edge of MIL-100(Al) with the electron dose (cumulated doses, see SI); (b) the corresponding HAADF-STEM images and chemical maps obtained for peaks CL_2 and CL_3 at 10 ē/Å² and 310 ē/Å². Evolution with the electron dose for MIL-100(Fe) of (c) the oxygen K-edge (on the left) and iron $L_{2,3}$-edge (on the right) from 10 ē/Å² to 780 ē/Å² (single acquisition doses) and (d) the iron $L_{2,3}$-edge obtained for higher electron doses between 500 ē/Å² and 10^4 ē/Å² (cumulated doses, see SI). (e) HAADF-STEM image (at the top) of MIL-100(Fe) and the corresponding elemental map (at the bottom) showing the spatial distribution of iron at $2x10^3$ ē/Å². The grey lines are EEL spectra obtained for amorphous*

carbon in (a) and iron (III) oxide in (d), while the black spectrum in (a) and (c) corresponds to BTC analysed by near-edge X-ray absorption fine structure (Buck, M.; Zharnikov, M. personal communication, 2022). All spectra are unprocessed. The energy resolution is about δE = 40 meV for (a) δE = 800 meV for (c) and δE = 220 meV for (d). NanoMOFs spectra in (a) and (d) have been normalised to the integrated signal (details in SI). Chemical maps were obtained as described in SI, after denoising by principal component analysis. (b) and (e) are intensity maps of the corresponding features integrated over the grey areas in (a) and (d). The intensity scale has been normalised to compare chemical maps at a given dose in (b). The spatial resolution is 10 nm in (b) and 2 nm in (e). More details are provided in SI.

In **Figure 3b**, we mapped the distribution of carbonyl components produced under the beam with a nanoscale spatial resolution, across the same scanned area, as a function of the electron dose (see SI for details and Figure S3). To do so, the intensities of peaks CL_2 and CL_3 were integrated, after background subtraction and processing with principal component analysis (PCA). At low-dose, carboxyl groups (-COO) are homogeneously distributed across the nanoparticles, as expected from the nanoMOFs molecular structure. At 310 $\bar{e}/Å^2$, a uniform reduction of the linker into carbonyl (-CO) is observed at this spatial resolution. Note that for such electron doses, the nanoparticle morphology remains unchanged, as observed in the corresponding HAADF image (left side). These results demonstrate the possibility of damage-free mapping at the nanoscale of specific chemical groups. Moreover, it should be mentioned that, to the best of our knowledge, intact organic component mapping has never been performed at an electron dose as low as employed here (10 $\bar{e}/Å^2$).

To correlate the linker's and metal's behaviour induced by the electron beam, we used a 400 eV energy window to acquire simultaneously the oxygen K-edge and Fe $L_{2,3}$-edge of MIL-100(Fe). The spectra were calibrated according to a previous X-ray Absorption Near-Edge Structure (XANES) study on MIL-100(Fe).[41] In agreement with the carbon K-edge, the oxygen K-edge of MIL-100(Fe) shows the degradation of the organic part under irradiation (**Figure 3c**, left side, red lines). At low-dose (10 $\bar{e}/Å^2$), it displays two peaks at 532.2 eV (denoted CL_5) and ~ 540 eV (denoted CL_7). These features are in agreement with XANES data obtained from

MIL-100(Fe)[41,42] and with NEXAFS measurements from free-standing BTC (comparison shown in **Figure 3c, black line**), where authors attributed the peaks to 1s–$\pi^*_{C=O}$ (CL_5) and 1s–σ^*_{C-O} (CL_7) transitions of carboxyl groups, respectively.[31] As the metal-linker coordination bond is achieved through oxygen elements of carboxylate groups, one could expect additional features related to iron coordination. Indeed, the Fe*(3d)*-O*(2p)* orbital hybridisation[43] should be detected near 531.5 eV, as typically observed in EELS for iron (III) oxide (whose oxygen K-edge is shown in Figure S2). Here, its absence for MIL-100(Fe) is probably due to the lower concentration of iron-oxo clusters compared to carboxylic linkers (two linkers per cluster as indicated by the molecular formula $Fe_3O(OH)(BTC)_2(H_2O)_2$). Moreover, the oxygen K-edge analysis at low-dose (10 $\bar{e}/Å^2$) remains limited by its low cross-section, as observed in **Figure 3c,** where the fine structure analysis is hindered by the low SNR.

Upon irradiation, peak CL_5 decreases attesting to the damage of the -COO bonds. In the meantime, the asymmetric peak CL_6 appears near 534.2 eV. The identification of this peak is not straightforward. Previous studies based on NEXAFS and EELS have attributed a similar peak to 1s–$\pi^*_{C=O}$, 1s–π^*_{C-OH} or 1s–$\sigma^*_{C=O}$ transitions in BDC,[32] amino-acids,[44] oxidised multi-walled carbon nanotubes[45] and poly(ethylene terephthalate).[46] These multiple assignments make it difficult to identify the peak CL_6 reliably. Nonetheless, our present results on the carbon K-edge strongly suggest that the peak CL_6 is associated with the reduction of carboxylic groups into carbonyl. Indeed, we observe a concurrent increase of the peaks CL_2 and CL_6 above 30 $\bar{e}/Å^2$. As we assign the CL_2 peak to carbonyl groups (-CO), the CL_6 peak could also highlight the degradation of the linkers' -COO groups.

Thereafter, we studied the metal part of nanoMOFs and first kept focused on MIL-100(Fe) (**Figures 3c and 3d**). **Figure 3c (right side, red lines)** depicts the typical dose evolution observed for the iron $L_{2,3}$-edge on MIL-100(Fe). The L-edges of transition metals provide information on their electronic environment such as oxidation state and crystal-field splitting.[43]

Unfortunately, the signal was found to be too low in low-dose conditions for any fine analysis. Iron's low cross-section and low concentration in the nanoMOFs make the signal tens of times weaker than the carbon K-edge one. A quantifiable signal was only detected for higher electron doses starting from 90 $\bar{e}/Å^2$. As aforementioned, these conditions imply that the organic part is already degraded. At this dose, MIL-100(Fe) exhibit a main peak at 707.6 eV, followed by a small shoulder at 708.9 eV observable for higher electron doses (i.e. 780 $\bar{e}/Å^2$). These data agree with previous XANES measurements on MIL-100(Fe) where authors attributed the signature to surface Fe^{2+} species produced by reduction under vacuum.[41,42] These authors also detected a peak at 534.2 eV similar to CL_6, which we assign here to degraded organic linkers. Herein, the combined systematic study of the iron, oxygen and carbon edges as a function of the electron dose provides supplementary information on this phenomenon. This dose-effect study suggests that the linkers' reduction induced by radiolysis can also affect the coordination structure of iron and hence, its valency. Nonetheless, the iron behaviour under high electron irradiation remains unclear. **Figure 3d** shows the evolution of the iron $L_{2,3}$-edge of MIL-100(Fe) compared to an iron(III) oxide reference (grey line) for higher doses between 500 $\bar{e}/Å^2$ and 10^4 $\bar{e}/Å^2$. Starting from $2x10^3$ $\bar{e}/Å^2$, the peak of MIL-100(Fe) located at 708.9 eV drastically increases revealing changes in electronic configuration. For this high dose range, the organic fraction is drastically degraded and may involve a complex chemical evolution which is not straightforward to disentangle.

Figure 3e shows the elemental iron map achieved by integrating the L_3-edge signal after PCA processing (details in SI). It attests to a homogeneous distribution of iron across the nanoMOFs, with a spatial resolution of 2 nm. Iron valency distribution could not be mapped at low doses because of its weak SNR features and, for higher electron doses, its distribution analysis is irrelevant since the nanoMOFs are degraded. Other metallic edges of nanoMOFs were also detected in the same conditions. Figure S4 shows the iron $M_{2,3}$-edge of MIL-100(Fe) and

zirconium $M_{2,3,4,5}$ and $N_{2,3}$-edges of UiO-66. For MIL-100(Al), the aluminium K and $L_{2,3}$-edges typically located at 1560 eV and 77 eV were not detected, probably due to their low cross-section and low aluminium concentration in the specimen.

Our results provide insights into the nanoscale analysis of intact complex organic assemblies. Compared to the commonly used soft X-ray absorption spectromicroscopies,[30] EELS provides a similar fine structure analysis with high energy resolution features, closely similar to the XANES and NEXAFS studies, but also enables a low-dose chemical mapping of the linkers functions with an improved spatial resolution[6] down to 10 nm (**Figure 3b**). These results demonstrate the possibility of characterising intact sensitive specimens at the nanoscale.

Low-loss excitations

Thereafter, we focus on analysing the LL region, where the excitations of valence electrons are visible. First, we used a large energy window of 400 eV to simultaneously monitor the LL and CL evolutions with the electron dose (**Figure 4a-c**, δE = 800 meV). Then, we used a smaller energy window, spanning 16 eV, to achieve a better energy resolution (**Figure 4d**, δE = 40 meV). The more significant LL contribution shared for the three nanoMOFs is a huge bulk plasmon peak standing out near 22 eV, which is due to the electrons' collective oscillations (observed in **Figure 2b**). As shown in **Figure 4a-c**, other molecular are also observable in the UV energy range below 10 eV. Unlike the carbon K-edge that is similar for the three systems, distinct LL features are found for each nanoMOF. **Figure 4d** shows the low-loss response of nanoMOFs obtained at low (10 $\bar{e}/Å^2$) and higher (above 130 $\bar{e}/Å^2$) electron doses with a closer look between 2 eV and 10 eV. At low-dose, MIL-100(Al) displays an intense peak centred around 5.8 eV with shoulders at 5.2 eV and 6.6 eV. For MIL-100(Fe), a similar feature is exhibited with a slight blue shift of the intense peak to 5.9 eV and less pronounced shoulders at 5.3 eV and 6.6 eV. Both MIL-100 exhibit two weak features at 2.5 eV and 3.5 eV and an

additional very weak peak near 4.5 eV. Conversely, only two intense and asymmetric peaks are found for UiO-66 near 5.1 eV and 6.5 eV. The aforementioned signals of the three nanoMOFs agree reasonably well with UV-vis experiments between 2 eV and 6 eV.[47–49] They have been usually related to π–π* transitions but barely assigned to specific chemical functions. To get more insights, we compared the signature of nanoMOFs with their free-standing organic linkers, focusing on the shaded area LL_2 in **Figure 4a-d**. The two organic linkers (BTC and BDC) show two peaks at 5.3 eV and 6.8 eV (see Figure S5 for the comparison of nanoMOFs, BTC and BDC spectra). They were attributed to the designated benzoic and local-excitation bands of functionalised phenyl groups, respectively.[50] These bands seem to be slightly red-shifted for nanoMOFs, where the linkers are coordinated with metals (e.g. shifted to 5.1 eV and 6.5 eV for UiO-66). Hence, we assume that the metal bonding affects the LL_2 features of the coordinated organic molecules. This is in agreement with previous UV-vis studies that related the 5.1 eV peak of UiO-66 to linker-to-metal charge transfer.[51–53] In addition, the peak observed for MIL-100 around 5.8/5.9 eV is not detected for the organic linkers. Thus, this intense peak may also be related to metal bonding. In a nutshell, our results suggest the LL_2 feature may be considered as a spectral fingerprint of the coordination bonding between the organic and metal parts of the nanoMOFs. In the absence of UV-vis data from the literature, the weak features observed for MIL-100 below 4 eV are not straightforward to interpret and theoretical studies are required in order to elucidate their origin.

As already noticed in the carbon K-edge study, the LL signal displays particular changes upon electron irradiation. As shown in **Figure 4a-d**, all the LL_2 features decrease with the electron dose. A more detailed evolution with the electron dose can be found in Figure S5. Considering our assignment, this can reveal the loss of coordination bonds between metal clusters and organic linkers that are progressively degraded. In the meantime, a peak near 4 eV (denoted LL_1) rises with the electron dose. Previous EELS and UV-vis studies of the

polymethylmethacrylate degradation induced by irradiation have attributed this peak to the formation of carbonyl functions ($n–\pi^*_{C=O}$ transitions).[54,55] The simultaneous acquisition of the LL and CL signals (400 eV energy window) allows us to compare their evolution. **Figures 4a-c**, S1 and S5 show the concurrent formation of peaks LL_1 and CL_2 with the decrease of LL_2 features for doses above 130 $\bar{e}/Å^2$. These observations suggest that the loss of coordination bonds is related to the reduction of carboxylic groups (-COO) into carbonyl moieties (-CO). Indeed, as the nanoMOFs assembly is conducted by the coordination of the carboxylic functions, their reduction into carbonyl species weakens the coordination bond, inducing the decrease of the features LL_2.

Interestingly, the three nanoMOFs display a similar peak near 9 eV (denoted LL_3, **Figure 4d**), which is red-shifted to 8.4 eV upon irradiation (see Figure S5). Such a peak has previously been attributed to water exciton.[36,56] Its presence for MIL-100 could be related to structural water as indicated by the chemical formula $(Al_3O(OH)(BTC)_2(H_2O)_2$ and $Fe_3O(OH)(BTC)_2(H_2O)_2)$. But, considering water molecules to be prone to beam degradation,[57] it could also be attributed to hydroxyl groups (-OH), also present in the three nanoMOFs (UiO-66 chemical formula: $Zr_6O_4(OH)_4(BDC)_6$). Another peak near 14 eV is also observable for electron doses above 80 $\bar{e}/Å^2$ (**Figure 4a-c**). As previously reported,[36,58] it is associated with the hydrogen K-edge, attesting to the production of H_2 upon electron irradiation. Since we assume direct dehydrogenation of the organic linkers even at low-dose (no $1s–\sigma^*_{C-H}$ transitions are observed in our carbon K-edge data), the dihydrogen signal certainly comes from the hydroxyl groups or structural water of nanoMOFs. Noteworthy, it suggests that irradiation of hydroxyl groups and structural water may enhance the beam-induced degradation effect as (i) it could produce reactive species such as radicals, which may increase the radiolysis of the organic linkers[36] and (ii) lead to complex chemical evolution affecting the metal environment (e.g. change of the iron $L_{2,3}$-edge for high electron doses in Figure 3d).

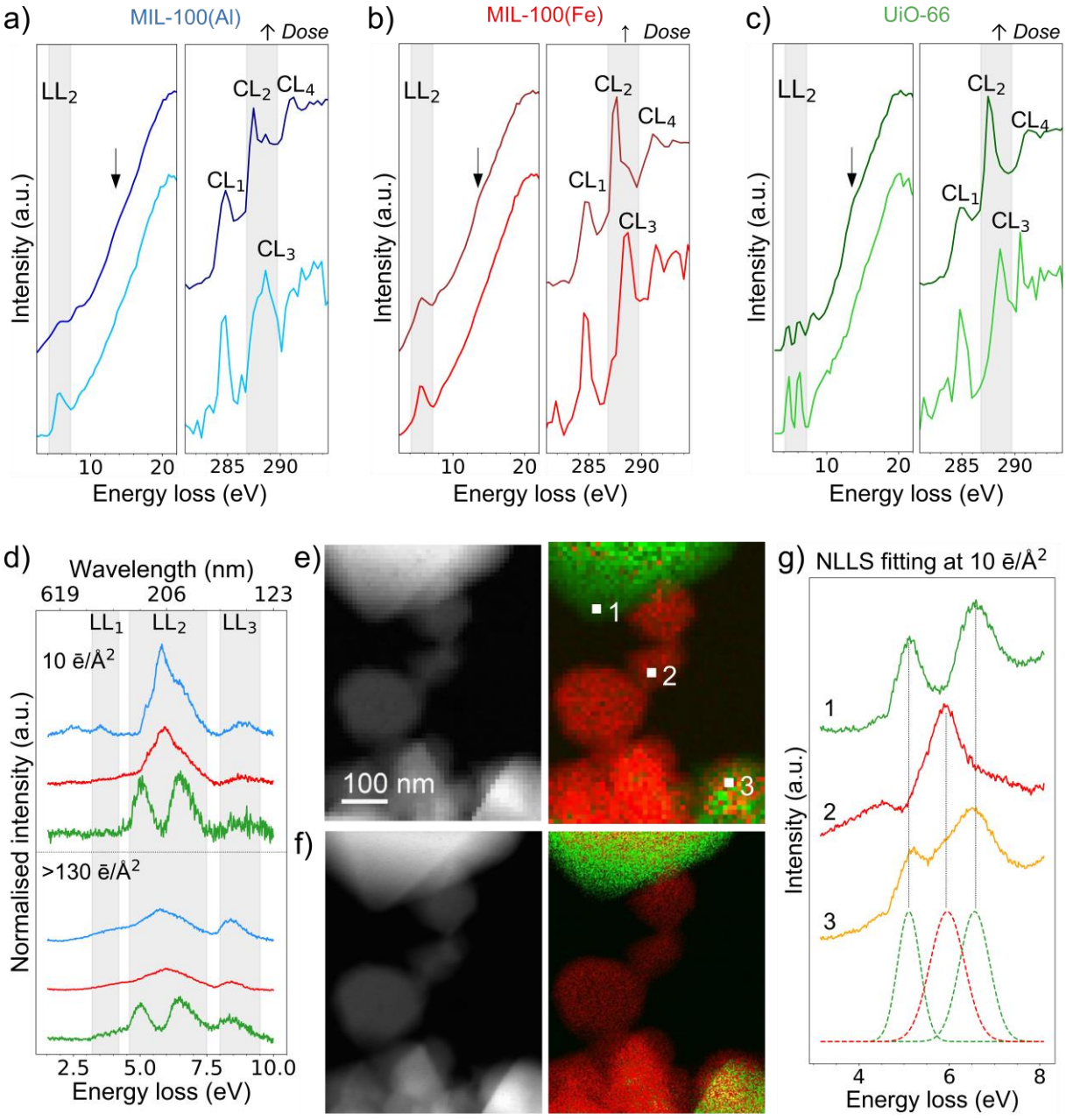

Figure 4. *Low-loss analysis of MIL-100 and UiO-66 nanoparticles as a function of the electron dose. (a-c) Evolution with the electron dose of the low-loss signal acquired simultaneously with the carbon K-edge using the 400 eV energy window. The energy resolution is about δE = 800 meV. The electron doses are 10 ē/Å^2 for light colours and >750 ē/Å^2 for dark colours (single acquisition doses, see SI). Black arrows near 14 eV indicate the H K-edge revealing H_2 production under irradiation. (d) Comparison of the low-loss signal obtained at electron dose of 10 ē/Å^2 (top row) and above 130 ē/Å^2 (bottom row) (cumulated doses, see SI) with a smaller energy window spanning 16 eV (energy resolution of about δE = 40 meV). Spectra are normalised to the integrated signal (see SI). (e-f) HAADF-STEM images (left) and the corresponding maps (right) of UiO-66 (green) and MIL-100(Fe) (red) obtained at (e) 10 ē/Å^2 and (f) 210 ē/Å^2 after PCA processing. The pixel size is 10 nm in (e) and 2 nm in (f). (g) Spectra obtained after PCA (solid lines) from the areas labelled 1, 2, and 3 in (e) and the NLLS components (dashed lines) used to map their distribution. Spectra of (a-d) are average raw data obtained by extracting and summing the signal over hundreds of square nanometres. Blue,*

red and green represent MIL-100(Al), MIL-100(Fe), UiO-66 in (a-g) while orange line stands for the superimposed signal of the latter two in (g). SI provides more details.

Recent studies have reported about damage-free LL EELS signatures of organic specimens[11,17] but none of them provides maps of the signals. Conversely, other authors used higher electron doses to map the signal of MOF glass blends,[16] probably inducing beam damages. Here, a specimen was prepared by mixing MIL-100(Fe) with UiO-66 and LL maps were recorded at low-dose to ensure nanoMOFs being intact (**Figure 4e-f**). As shown in **Figures 4e and 4g**, each nanoMOF specific feature was mapped at 10 $\bar{e}/Å^2$, using PCA processing and Nonlinear Least-Squares (NLLS) Gaussian fitting (details on the NLLS Gaussian fitting are provided in SI, Figure S6). To assess the possibility of localising the two signals at higher electron doses, the study was repeated at 210 $\bar{e}/Å^2$ (**Figure 4f**). In the two conditions, MIL-100(Fe) (in red) was successfully distinguished from UiO-66 (in green). This result demonstrates that the chemical information can still be localised despite degradation under electron irradiation. The main difference between the two conditions lies in the spatial resolution: the lowest electron dose, associated with no degradation, imposes a large pixel size of 10 nm, whereas fixing a higher dose allows an increase of the pixel size to 1 nm but induces beam damage. This highlights the general trend that the chemical imaging of sensitive nanomaterials is a trade-off between spatial resolution and induced degradation. Our results illustrate the possibility of distinguishing organic molecules in the LL energy range and mapping their features with a nanoscale resolution.

By correlating the CL and LL energy ranges, our results enable deciphering the chemical changes induced by electron irradiation. To a lesser extent, the chemical changes under irradiation have previously been studied for MOFs in the LL and CL.[10] Here, with low-dose conditions and an improved energy resolution, we further demonstrate that it is possible to distinguish the direct beam effect (reduction of carboxylic moieties, radiolysis of hydroxyl

groups and H_2 production) from the secondary reactions implied (loss of coordination bond and iron reduction). Nonetheless, since EELS allows one to reach energy ranges that are arduously covered by conventional techniques (e.g. VUV, XUV), all our assignments remain assumptions that need to be confirmed with theoretical studies.

Ultralow-loss excitations

The three nanoMOFs and their free-standing organic linkers were analysed in the vibrational energy window with conventional attenuated total reflection (ATR) – Fourier Transform (FT) IR and ULL STEM-EELS. The energy resolution was equal to 4 cm^{-1} for FTIR and 12 meV (97 cm^{-1}) for EELS. By applying the Richardson-Lucy deconvolution (details in SI and Figure S7), the EELS ZLP was narrowed to reach an energy resolution of δE = 7 meV (55 cm^{-1}). **Figure 5a** compares the resulting spectra obtained with the two techniques. The full spectra ranging from 70 meV to 500 meV are given in Figures S8 and S9. Here, we briefly describe the main vibrational modes denoted from ULL_1 to ULL_6 (grey areas in **Figures 5a**, S5 and S6) but a complete assignment based on the literature can be found in Table S1.

FTIR spectra display the features specific to the specimen's functional groups (**Figure 5a**). In the ULL_2 area, characteristic bands of the metal part are observed for MIL-100(Fe) and UiO-66. For MIL-100(Fe), the asymmetric Fe_3-μ_3-O stretching band is located at 624 cm^{-1} (77 meV). Noticeably, this band carries information on the oxidation state of iron: a previous FTIR study has demonstrated that the partial reduction of iron induces a blue shift of this band from 618 cm^{-1} to 597 cm^{-1}.[59] Here, our FTIR data indicate that non-irradiated MIL-100(Fe) contain Fe^{3+} ions, in agreement with previous Mössbauer studies.[60] Likewise, the Zr_3-μ_3-O stretching bands of UiO-66 are observed at 620 – 745 cm^{-1} (80 - 90 meV), where they are mixed with the vibration modes of the organic part. The five specimens display significant bands in the ULL_4 area. They are attributed to CO stretching modes of carboxylic groups. By comparing the

nanoMOFs with their organic linkers, these bands seem to shift upon coordination. Whereas the BTC CO bands are located at 1326 cm^{-1} (164 meV) and 1691 cm^{-1} (210 meV), they are found at 1405 cm^{-1} (174 meV), 1672 cm^{-1} (207 meV) for MIL-100(Al) and 1380 cm^{-1} (171 meV), 1632 cm^{-1} (202 meV) for MIL-100(Fe). Similarly, CO bands are red-shifted from 1287 cm^{-1} (160 meV) and 1682 cm^{-1} (209 meV) in BDC to 1387 cm^{-1} (172 meV) and 1584 cm^{-1} (196 meV) in UiO-66 (see Table S1). This comparison also highlights the distinct features of BDC, which exhibits additional bands in the ULL3 area corresponding to CC, CO and CH bending modes. In the three nanoMOFs spectra, residual solvents (water, ethanol and N,N-dimethylformamide, DMF) are also detected. More details are given in Figure S8.

In EELS data, the main specific ULL features observed for the five specimens are in agreement with the FTIR results (**Figure 5a**). Given the lower energy resolution, all the peaks cannot be observed, but the metal and carboxylic main features were readily detected. The CH bending (ULL_2 area) and CO stretching modes (ULL_4 area) match the FTIR experiments for all the specimens except BTC. Indeed, the EELS intensity of the BTC CO band (215 meV, 1734 cm^{-1}) seems reduced compared to FTIR. Such spectral differences between the two techniques may be explained by distinct excitation mechanisms following photons absorption (FTIR) and electrons inelastic scattering (EELS). Nevertheless, a complete understanding will need the help of theoretical calculations. At high energy losses, the features detected in EELS as in FTIR can be attributed to the remaining solvents (adsorbed DMF, ethanol and structural water). A more detailed discussion is provided in Figure S9. Beyond the similarities with the FTIR signal, EELS reveals additional vibrational excitations at low energy (ULL_1 peaks) that were not reached with the conventional technique (**Figure 5a**). Al-O, Fe-O and Zr-O stretching modes of MIL-100(Al), MIL-100(Fe) and UiO-66 were recorded in the far IR region at 71 meV (573 cm^{-1}), 60 meV (484 cm^{-1}) and 64 meV (516 cm^{-1}), respectively (assignment based on the literature as cited in Table S1).

Despite the generally good agreement between FTIR and EELS data (**Figure 5a**), minor differences were observed. Indeed, the ULL study was performed at electron doses around 120 $\bar{e}/Å^2$ to increase the SNR and, based on the carbon K-edge analysis (**Figure 3a**), these conditions induce chemical damage to the specimens. Effective evidence lies in the peak found in EELS at 291 meV (2347 cm^{-1}) for the nanoMOFs (indicated in Figure S9 with an arrow) that was not detected in FTIR (Figure S8) and can correspond to degraded products. Moreover, it must be mentioned that all the aforementioned bands (**Figure 5a**) may be slightly shifted from their initial positions due to partial degradation of the chemical functions. For instance, the CO stretching modes (ULL_4 peaks) could correspond to degraded carboxylic (COO) groups, or even carbonyl (CO) groups, as demonstrated in the carbon K-edge study. Given the EELS' limited energy resolution, such subtle differences cannot be discriminated.

Recent studies have suggested a possible damage-free analysis of sensitive specimens in the ULL energy range using the aloof configuration.[11–13,61,62] By focusing the electron probe a few nanometers away from the specimen, the authors recorded an intact signal. This configuration leverages the long-range interactions associated with the phonon excitations to collect a signal without direct impact on the specimen.[7] Here, measurements were repeated in transmission and aloof configurations, and no differences were observed apart from a lower SNR (see Figure S10). This points out an interesting fact: here, EELS performed in the transmission (bulk excitation) and the aloof modes give peaks at sensibly the same energy revealing an absence of dispersion effect. Collective excitations (e.g. surface phonon polaritons) would implied a dispersion effect, and its absence here indicates the excitation of very localised vibrational modes associated with molecular vibrations. As a further evidence, we did not observe the rapid surface signal intensity modulation characteristic of confined surface phonon polaritons in phononic nanomaterials.[63] Thereafter, the transmission configuration was chosen for our

experiments because, compared to the aloof one, it offers the possibility of a spatially resolved analysis, allowing chemical mapping.

By using the transmission configuration, previous studies have mapped the linker signature of MOF crystal-glass composites, notably constituted of BDC.[14] Yet, while employing higher electron doses (below $5x10^3$ $\bar{e}/Å^2$), their analysis was still affected by the difficulty of ZLP tail removal. Herein, with lower electron doses (~120 $\bar{e}/Å^2$), we provide a chemical map of the MIL-100(Al) linkers' distribution at a pixel size of 2 nm. To do so, we chose the MIL-100(Al)'s CO stretching modes since they are the most intense features of the spectra. Despite their possible degradation, they remain an appropriate and robust spectral fingerprint of the nanoMOFs vibrational excitations. **Figure 5b-c** displays the HAADF image and chemical map obtained by integrating the intensity of the two CO bands (ULL_4 peaks) after background subtraction and PCA processing (see SI). To exclude any contribution from the nanoparticles thickness, the chemical map has been normalised by the ZLP intensity. An enhanced signal is detected on the nanoMOFs. **Figure 5d** provides averaged intensity line profiles of the HAADF (in black) and chemical map images (in blue) measured in the white dotted rectangle. The HAADF and chemical signals are clearly correlated. A weaker signal is also found on the amorphous carbon film (grey area in the HAADF image of **Figure 5b**, and indicated by grey stars in the line profile of **Figure 5d**) due to excitations in the ULL_4 area (Figure S9).[64] Finally, a map was obtained with a similar data processing from an energy range with no excitations (450 – 495 meV) and no signal was detected (**Figure 5e**). All together, these results attest to the effective localisation of the CO vibrational modes on the nanoMOFs. They demonstrate the possibility of mapping the vibrational excitations of sensitive nanoMOFs with high energy and spatial resolution. Compared to IR spectromicroscopy, EELS provides similar information on the molecular vibrational modes, but it also allows mapping their distribution with an improved spatial resolution (at the nanoscale).

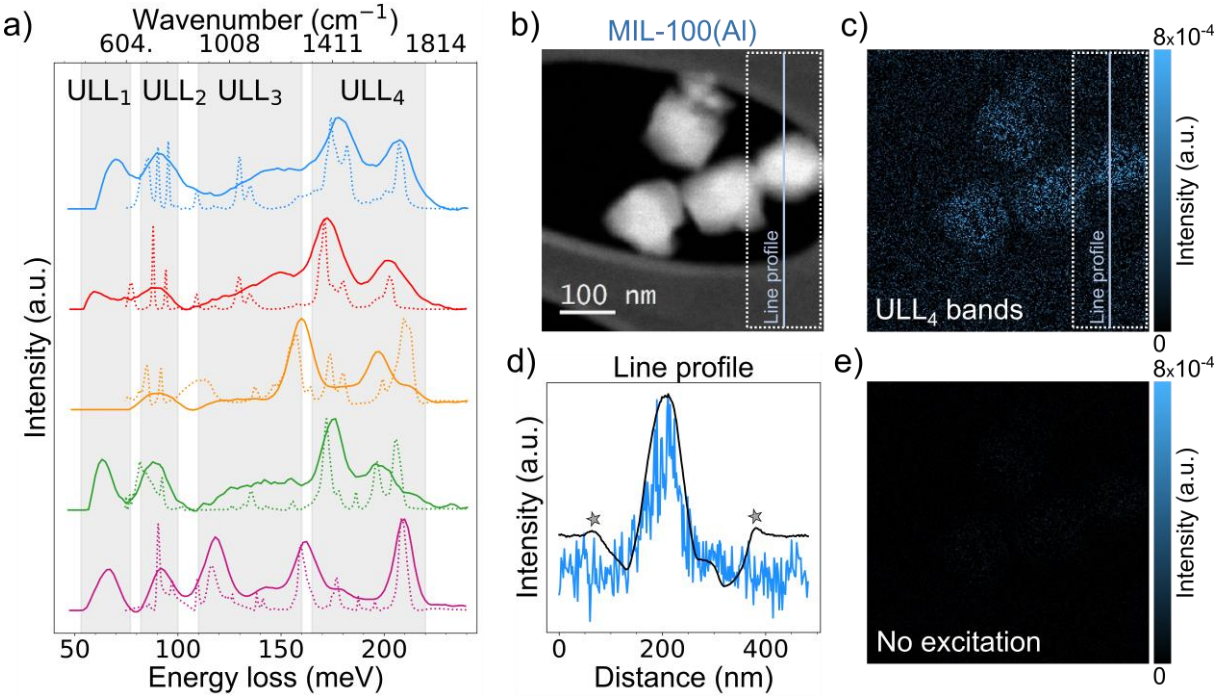

Figure 5. *Ultralow-loss analysis of nanoMOFs and their free-standing organic linkers acquired at about 120 ē/Å^2 (single acquisition dose, beam current = 4 pA, total acquisition time ~ 100s). (a) Comparison of the ultralow-loss EELS (solid line) with conventional FTIR (dotted line) for MIL-100(Al) in blue, MIL-100(Fe) in red, BTC in yellow, UiO-66 in green and BDC in pink. All EEL spectra are averages obtained by extracting and summing the signal over the whole hyperspectral image. They have been collected in an energy window of 2 eV and deconvolved using the Richardson-Lucy Algorithm (details in SI). The EEL energy resolution is about δE = 7 meV (55 cm^{-1}), and the FTIR one is about 4 cm^{-1} (0.5 meV). (b) HAADF image of MIL-100(Al) nanoparticles and (c) the corresponding chemical map of the CO vibration modes (shaded ULL$_4$ area in (a)). (d) Intensity profiles acquired along the indicated line of the HAADF image (black line profile) and the chemical map (blue line profile) from (b-c). To increase the SNR, several line profiles were added, as illustrated by the white dotted rectangle in (b-c). It shows a localised signal on the nanoparticles. Grey stars indicate the amorphous carbon film signal. (e) Chemical map obtained on an area where no excitation was detected (450 – 495 meV). It attests thickness does not contribute to the signal map of MIL-100(Al) in (b). The pixel size is 2 nm in (b-c) and (e). Chemical maps were obtained as described in SI. They have been normalised to the ZLP to exclude the thickness variations. For comparison, their intensity scale is also normalised (see SI).*

Monitoring beam-induced chemical reactions.

The present study has allowed us to monitor the chemical degradation of three sensitive nanoMOFs under electron irradiation. Thanks to the multimodal approach, we have assigned all the vibrational and electronic transitions observed in the IR, UV and soft X-ray energy ranges to specific functional groups. In **Figure 6**, we resume the schematic representation of

the nanoMOFs chemical structure given in **Figure 1d** and we indicate the corresponding peaks described in this manuscript according to the electron dose. The multimodal information was cross-correlated between the three energy windows to obtain a deep characterisation of nanoMOFs. For instance, at low-dose, while the metal-linker coordination bonding is not observed in the CL, it is well documented in the LL and ULL regions (peaks LL_2, ULL_1 and ULL_2). Upon irradiation, LL and CL features illustrate radiolysis damages to the organic linkers through (i) instantaneous dehydrogenation of the benzene ring, (ii) breakage of the benzene double bonds (peak CL_1) leading to the formation of single bonds (peak CL_4) and (iii) reduction of the carboxylic groups (-COO, peaks CL_3 and CL_5) into carbonyl composites (-CO, peak CL_2) causing the loss of coordination bond (peak LL_2). We suppose this linker vacancy leads to metal reduction. H_2 production under irradiation suggests (i) hydrogen loss from hydroxyl groups and remaining solvents (structural water, ethanol or DMF) and (ii) the formation of reactive species, such as radicals, that could enhance the beam-induced degradation effect through complex reactions. This mechanism remains an assumption that would need further investigations to be clarified.

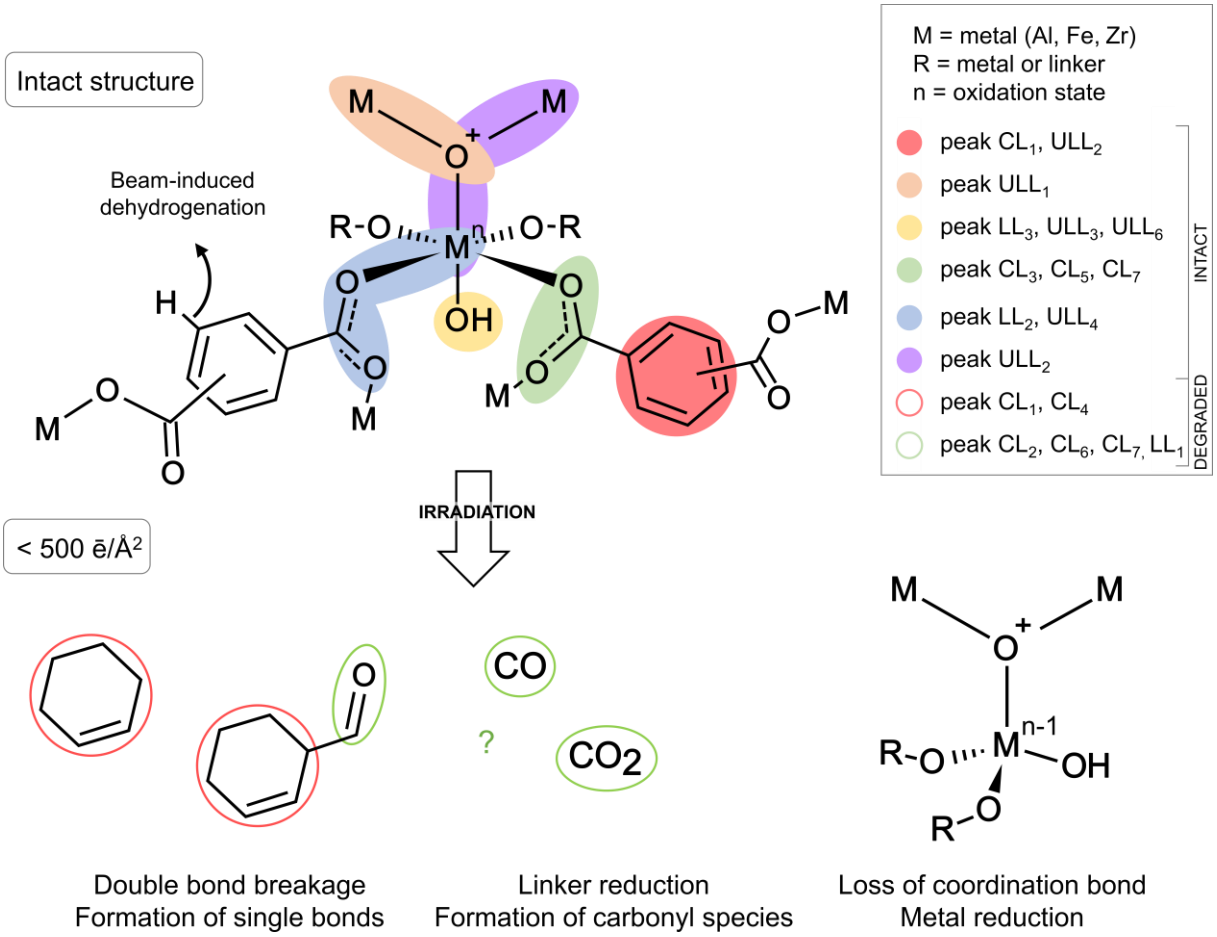

Figure 6. *Schematic representation of the main irradiation effects on the molecular structure of nanoMOFs. The different MIL-100 and UiO-66 structures have been simplified using general atom labels (M for metals and R for metals or linkers). At the top, the intact molecular structure of nanoMOFs depicts their characteristic chemical functions. The colours relate them to the peak assignment described in this manuscript and Table S1 for intact signatures, assuming that beam alteration is not detected in ULL EELS due to the energy resolution. At the bottom, the possible degraded structures are illustrated according to the observed alterations in EELS for doses below 500 ē/Å^2.*

CONCLUSION

This study presents a damage-free multimodal analysis of nanoMOFs at the nanoscale. Our results underline the powerful possibilities offered by STEM microscopes equipped with a monochromated beam and a direct electron detection in terms of energy resolution (down to 12 meV) and sensitivity for studying beam-sensitive specimens. The detector high dynamic range enables the analysis of very low signals obtained in low-dose conditions[22] and a multimodal

analysis with the simultaneous acquisition of the LL and CL signals without saturation from the ZLP. With low-dose (10 $\bar{e}/Å^2$) and cryogenic conditions, as employed for cryo-TEM high-resolution imaging of biological specimens, we successfully revealed the intact signatures of nanoMOFs and related them to specific electronic transitions. In these conditions, we outlined the spectral similarities between EELS and photon-based spectroscopic techniques. In the IR window, the vibration modes agreed with FTIR data acquired on the same specimens, albeit less energy resolved. In the X-ray window, the fine structure analysis revealed features very similar to the X-ray absorption spectroscopy data described in the literature. Besides, since EELS covers a broader energy range compared to photon-based spectroscopies, it has access to energy domains that are arduously reached by other techniques such as vacuum UV (100 – 200 nm, 6 – 12 eV) and extreme UV (10 – 100 nm, 12 – 120 eV) and are of main interest for investigating the valence electron excitations. Namely, we revealed valuable information on the metal-linker coordination bond in the vacuum-UV range, which precise identification needs to be specified by theoretical studies. Furthermore, at low-dose, we successfully mapped the distribution of the nanoMOFs' intact chemical groups in the three energy ranges, with a 10 nm spatial resolution. Then, since low-dose constrained the analysis spatial resolution, we demonstrated that higher electron doses could be employed to map the LL signal of MIL-100(Fe) and UiO-66 with a smaller pixel size (2 nm), without impeding the localisation of the chemical signature. By increasing the electron dose from 10 $\bar{e}/Å^2$ to 10^4 $\bar{e}/Å^2$, we monitored the irradiation-induced effect on these sensitive specimens in the three energy ranges and identified the chemical groups of intact and degraded signatures.

This study demonstrates STEM-EELS as a key technique for understanding the complexity of highly sensitive nanostructures, offering the possibility of a deep characterisation in a wide energy range, spanning from IR through UV to soft X-rays, in a single experiment. Our results outline that this multimodal approach allows the identification and mapping of the functional

groups of organic-inorganic specimens. Similar procedures could also be used to study other hybrid specimens of various compositions such as organic blend components, organic-inorganic interfaces or nanoparticles embedded in organic matrices or in the cellular context, but also pure organic materials as biological macromolecules or cellular organelles. Not only can products be identified, but chemical reactions can also be monitored to decipher complex mechanisms. Therefore, chemical reactions in nanosystems, including the most sensitive ones as hybrid or organic materials, could also be investigated *in situ* when changing the temperature (heating/cooling chip devices), the environment (liquid or gas reaction cells) or under irradiation (photons or electrons). In the following, we aim to investigate nanoMOFs as drug nanocarriers by characterising the drug loading and distribution and unveiling the cellular fate of single nanoparticles.

EXPERIMENTAL SECTION

NanoMOFs preparation. MIL-100(Fe) and MIL-100(Al) were synthesised following the previously reported microwave-assisted hydrothermal method.[65] UiO-66 nanoparticles were synthesised following the procedure described in [25]. In order to assess their purity, the three nanoMOFs were analysed after their synthesis and prior to nanoscale characterization, by Fourier Transform IR Spectroscopy (FTIR) in the attenuated total reflection (ATR) mode (Figure S8). Synthesis and specimen preparations are detailed in SI.

Cryogenic Transmission Electron Microscopy (cryo-TEM). The experiments were performed at 200kV on a JEOL JEM-2010 transmission electron microscope equipped with a *Schottky* field emission gun, a Gatan 626 cryo-holder and a Gatan Ultrascan 4K CCD camera. The specimens were imaged with a magnification of 50kx and 80kx using a minimal dose

system estimated between 10 and 15 ē/Å^2. Images were collected between 1000 nm and 2500 nm nominal defocus. All the results presented here are unprocessed.

Scanning Transmission Electron Microscopy and Electron Energy Loss Spectroscopy (STEM-EELS). STEM-EELS experiments were carried out on a monochromated Cs-corrected Nion Hermes 200-S microscope operated at 100kV, equipped with a single tilt cryo-specimen holder (HennyZ), a Nion Iris spectrometer and a Merlin Direct Electron Detector camera (Quantum Detectors, UK) for spectroscopic analysis. The convergence semi-angle was set to 10 mrad, enabling a sub-nanometer beam size. The spectra were recorded for each characteristic feature in different energy windows by adjusting the range to either 2 eV (dispersion of 1.6 meV/channel) or 16 eV (15.2 meV/channel) or 116 eV (112 meV/channel) or 400 eV (389 meV/channel). The entrance aperture for EELS was set to 300 µm for the 2 eV energy window and to 1 mm for the others. For each dispersion, the energy resolution δE was measured from the full-width at half-maximum of the ZLP. It reached 12 meV for the lowest energy window spanning 2 eV. Electron dose effects were analysed for a total dose from 10 ē/Å^2 to 10^4 ē/Å^2 and dose rates ranging from $4x10^3$ ē/Å^2/s to 10^6 ē/Å^2/s (details on total dose and dose rates are given in SI). This study has been performed by either a single acquisition on different areas or several successive acquisitions on the same area. The increasing single acquisition doses have been obtained by raising the probe current (from 6 pA to 40 pA), the dwell time (from 2 ms to 3 ms) and reducing the pixel size (from 10 nm to 3 nm). The cumulated doses of successive acquisitions have been obtained at a constant beam current (6 pA or 15 pA), by varying the pixel size (from 10 nm to 1 nm) and dwell time (from 2 ms to 80 ms). More details are given in SI. As EELS imposes a maximum thickness to collect a signal, we limited the analysis to small nanoparticles (< 150 nm). Apart from the LL mapping, we selected those above the grid carbon film holes to avoid the carbon contribution to the measurements. All EELS data were acquired in the conventional transmission mode, except for the organic linkers in the ULL

energy range, which were analysed in the aloof configuration due to their large thickness. Additional EELS for iron (III) oxide reference spectra was performed on a Nion Ultrastem 200 operating at 100 kV with a probe semi-angle of 25 mrad, an EELS aperture of 2 mm and an EELS energy window of 200 eV. Details on data processing are given in SI.

Fourier-Transform Infrared (FTIR) spectroscopy. Conventional FTIR spectra were collected for each type of nanoMOFs, and their corresponding organic linkers with a Vertex 70 spectrometer (Bruker, Germany) equipped with an ATR device. Data were collected between 4000 cm^{-1} and 600 cm^{-1} with a 1.5 mm spectral aperture averaging 128 scans. The spectral resolution was equal to 4 cm^{-1} (0.5 meV). SI provides details on the data processing.

SUPPORTING INFORMATION

The Supporting Information is available free of charge at https://pubs.acs.org/doi/10.1021/acsnano.XXX.

Additional experimental details of the nanoMOFs synthesis and sample preparation, the dose-effect experiment and data processing, additional FTIR and EELS spectra in the three energy ranges and the table of assignments (PDF).

ACKNOWLEDGMENTS

This work has been partly supported by the National Agency for Research under the program of future investment TEMPOS CHROMATEM (Reference no. ANR-10-EQPX-50) and the European Union's Horizon 2020 research and innovation program (Grant no. 823717, ESTEEM3). For the cryo-TEM experiments, the authors acknowledge the financial support from the « Investissements d'Avenir » of the LabEx PALM (ANR-10-LABX-0039-PALM).

We thank the STEM team at the Laboratoire de Physique des Solides, particularly M. Tencé, M. Walls, S. Y. Woo and L. H. G. Tizei for discussions and help with the EELS experiments.

We are grateful to X. Li and all the NanoBio team from Institut des Sciences Moléculaires d'Orsay for kindly providing the UiO-66 specimen and helping with the synthesis, and to the CPSysBio team at the Institut Chimie Physique, in particular A. Dazzi, A. Deniset-Besseau and J. Mathurin, for allowing us access to the ATR-FTIR equipment.

We sincerely thank T. Okajima from the Aichi Synchrotron Radiation Center, M. Zharnikov from Heidelberg University and M. Buck from University of St Andrews for sharing their NEXAFS data on the free-standing organic linkers.

REFERENCES

(1) Vaghasia, R.; Savani, M.; Saini, B. Metal Organic Frameworks (MOFs) as an Adsorbent Material for CO2 Capture. In *Metal Nanocomposites for Energy and Environmental Applications*; Singh, S. P., Agarwal, A. K., Kumar, K., Srivastav, S. K., Eds.; Energy, Environment, and Sustainability; Springer: Singapore, 2022; pp 157–186. https://doi.org/10.1007/978-981-16-8599-6_7.

(2) Ahmad, S.; Abbasi, B. bin K.; Nazir, M. S.; Abdullah, M. A. Metal Organic Frameworks (MOFs) as Formidable Candidate for Pharmaceutical Wastewater Treatment. In *Inorganic-Organic Composites for Water and Wastewater Treatment: Volume 2*; Lichtfouse, E., Muthu, S. S., Khadir, A., Eds.; Environmental Footprints and Eco-design of Products and Processes; Springer: Singapore, 2022; pp 37–63. https://doi.org/10.1007/978-981-16-5928-7_2.

(3) Qin, Y.; Hao, M.; Li, Z. Chapter 17 - Metal–Organic Frameworks for Photocatalysis. In *Interface Science and Technology*; Yu, J., Jaroniec, M., Jiang, C., Eds.; Surface Science of Photocatalysis; Elsevier, 2020; Vol. 31, pp 541–579. https://doi.org/10.1016/B978-0-08-102890-2.00017-8.

(4) Sacchetti, A.; Rossetti, A.; Martí-Rujas, J. Chapter Three - Metal-Organic Frameworks (MOFs) for Sensing. In *Advances in Chemical Engineering*; Magagnin, L., Rossi, F., Eds.; Soft Robotics; Academic Press, 2021; Vol. 57, pp 91–122. https://doi.org/10.1016/bs.ache.2021.03.002.

(5) He, S.; Wu, L.; Li, X.; Sun, H.; Xiong, T.; Liu, J.; Huang, C.; Xu, H.; Sun, H.; Chen, W.; Gref, R.; Zhang, J. Metal-Organic Frameworks for Advanced Drug Delivery. *Acta Pharm. Sin. B* **2021**. https://doi.org/10.1016/j.apsb.2021.03.019.

(6) Chaupard, M.; de Frutos, M.; Gref, R. Deciphering the Structure and Chemical Composition of Drug Nanocarriers: From Bulk Approaches to Individual Nanoparticle Characterization. *Part. Part. Syst. Charact.* **2021**, *38* (9), 2100022. https://doi.org/10.1002/ppsc.202100022.

(7) Colliex, C. From Early to Present and Future Achievements of EELS in the TEM. *Eur. Phys. J. Appl. Phys.* **2022**, *97*, 38. https://doi.org/10.1051/epjap/2022220012.

(8) Egerton, R. F. Radiation Damage to Organic and Inorganic Specimens in the TEM. *Micron* **2019**, *119*, 72–87. https://doi.org/10.1016/j.micron.2019.01.005.

(9) Ilett, M.; S'ari, M.; Freeman, H.; Aslam, Z.; Koniuch, N.; Afzali, M.; Cattle, J.; Hooley, R.; Roncal-Herrero, T.; Collins, S. M.; Hondow, N.; Brown, A.; Brydson, R. Analysis of Complex, Beam-Sensitive Materials by Transmission Electron Microscopy and Associated Techniques. *Philos. Trans. R. Soc. Math. Phys. Eng. Sci.* **2020**, *378* (2186), 20190601. https://doi.org/10.1098/rsta.2019.0601.

(10) Ghosh, S.; Yun, H.; Kumar, P.; Conrad, S.; Tsapatsis, M.; Mkhoyan, K. A. Two Distinct Stages of Structural Modification of ZIF-L MOF under Electron-Beam Irradiation. *Chem. Mater.* **2021**, *33* (14), 5681–5689. https://doi.org/10.1021/acs.chemmater.1c01332.

(11) Rez, P.; Aoki, T.; March, K.; Gur, D.; Krivanek, O. L.; Dellby, N.; Lovejoy, T. C.; Wolf, S. G.; Cohen, H. Damage-Free Vibrational Spectroscopy of Biological Materials in the Electron Microscope. *Nat. Commun.* **2016**, *7* (1), 10945. https://doi.org/10.1038/ncomms10945.

(12) Haiber, D. M.; Crozier, P. A. Nanoscale Probing of Local Hydrogen Heterogeneity in Disordered Carbon Nitrides with Vibrational Electron Energy-Loss Spectroscopy. *ACS Nano* **2018**, *12* (6), 5463–5472. https://doi.org/10.1021/acsnano.8b00884.

(13) Hachtel, J. A.; Huang, J.; Popovs, I.; Jansone-Popova, S.; Keum, J. K.; Jakowski, J.; Lovejoy, T. C.; Dellby, N.; Krivanek, O. L.; Idrobo, J. C. Identification of Site-Specific

Isotopic Labels by Vibrational Spectroscopy in the Electron Microscope. *Science* **2019**, *363* (6426), 525–528. https://doi.org/10.1126/science.aav5845.
(14) Collins, S. M.; Kepaptsoglou, D. M.; Hou, J.; Ashling, C. W.; Radtke, G.; Bennett, T. D.; Midgley, P. A.; Ramasse, Q. M. Functional Group Mapping by Electron Beam Vibrational Spectroscopy from Nanoscale Volumes. *Nano Lett.* **2020**, *20* (2), 1272–1279. https://doi.org/10.1021/acs.nanolett.9b04732.
(15) Guo, C.; Allen, F. I.; Lee, Y.; Le, T. P.; Song, C.; Ciston, J.; Minor, A. M.; Gomez, E. D. Probing Local Electronic Transitions in Organic Semiconductors through Energy-Loss Spectrum Imaging in the Transmission Electron Microscope. *Adv. Funct. Mater.* **2015**, *25* (38), 6071–6076. https://doi.org/10.1002/adfm.201502090.
(16) Collins, S. M.; Kepaptsoglou, D. M.; Butler, K. T.; Longley, L.; Bennett, T. D.; Ramasse, Q. M.; Midgley, P. A. Subwavelength Spatially Resolved Coordination Chemistry of Metal–Organic Framework Glass Blends. *J. Am. Chem. Soc.* **2018**, *140* (51), 17862–17866. https://doi.org/10.1021/jacs.8b11548.
(17) Das, P. P.; Guzzinati, G.; Coll, C.; Gomez Perez, A.; Nicolopoulos, S.; Estrade, S.; Peiro, F.; Verbeeck, J.; Zompra, A. A.; Galanis, A. S. Reliable Characterization of Organic & Pharmaceutical Compounds with High Resolution Monochromated EEL Spectroscopy. *Polymers* **2020**, *12* (7), 1434. https://doi.org/10.3390/polym12071434.
(18) Pal, R.; Bourgeois, L.; Weyland, M.; Sikder, A. K.; Saito, K.; Funston, A. M.; Bellare, J. R. Chemical Fingerprinting of Polymers Using Electron Energy-Loss Spectroscopy. *ACS Omega* **2021**, *6* (37), 23934–23942. https://doi.org/10.1021/acsomega.1c02939.
(19) Liu, L.; Zhang, D.; Zhu, Y.; Han, Y. Bulk and Local Structures of Metal–Organic Frameworks Unravelled by High-Resolution Electron Microscopy. *Commun. Chem.* **2020**, *3* (1), 1–14. https://doi.org/10.1038/s42004-020-00361-6.
(20) Mayoral, A.; Mahugo, R.; Sánchez-Sánchez, M.; Díaz, I. Cs-Corrected STEM Imaging of Both Pure and Silver-Supported Metal-Organic Framework MIL-100(Fe). *ChemCatChem* **2017**, *9* (18), 3497–3502. https://doi.org/10.1002/cctc.201700519.
(21) Zhang, D.; Zhu, Y.; Liu, L.; Ying, X.; Hsiung, C.-E.; Sougrat, R.; Li, K.; Han, Y. Atomic-Resolution Transmission Electron Microscopy of Electron Beam–Sensitive Crystalline Materials. *Science* **2018**. https://doi.org/10.1126/science.aao0865.
(22) Hart, J. L.; Lang, A. C.; Leff, A. C.; Longo, P.; Trevor, C.; Twesten, R. D.; Taheri, M. L. Direct Detection Electron Energy-Loss Spectroscopy: A Method to Push the Limits of Resolution and Sensitivity. *Sci. Rep.* **2017**, *7* (1), 8243. https://doi.org/10.1038/s41598-017-07709-4.
(23) Li, X.; Porcino, M.; Qiu, J.; Constantin, D.; Martineau-Corcos, C.; Gref, R. Doxorubicin-Loaded Metal-Organic Frameworks Nanoparticles with Engineered Cyclodextrin Coatings: Insights on Drug Location by Solid State NMR Spectroscopy. *Nanomaterials* **2021**, *11* (4), 945. https://doi.org/10.3390/nano11040945.
(24) Li, X.; Semiramoth, N.; Hall, S.; Tafani, V.; Josse, J.; Laurent, F.; Salzano, G.; Foulkes, D.; Brodin, P.; Majlessi, L.; Ghermani, N.-E.; Maurin, G.; Couvreur, P.; Serre, C.; Bernet-Camard, M.-F.; Zhang, J.; Gref, R. Compartmentalized Encapsulation of Two Antibiotics in Porous Nanoparticles: An Efficient Strategy to Treat Intracellular Infections. *Part. Part. Syst. Charact.* **2019**, *36* (3), 1800360. https://doi.org/10.1002/ppsc.201800360.
(25) Morris, W.; Wang, S.; Cho, D.; Auyeung, E.; Li, P.; Farha, O. K.; Mirkin, C. A. Role of Modulators in Controlling the Colloidal Stability and Polydispersity of the UiO-66 Metal–Organic Framework. *ACS Appl. Mater. Interfaces* **2017**, *9* (39), 33413–33418. https://doi.org/10.1021/acsami.7b01040.

(26) Jeanguillaume, C.; Colliex, C.; Ballongue, P.; Teneé, M. New STEM Multisignal Imaging Modes, Made Accessible through the Evaluation of Detection Efficiencies. *Ultramicroscopy* **1992**, *45* (2), 205–217. https://doi.org/10.1016/0304-3991(92)90510-Q.
(27) Dubochet, J.; Lepault, J.; Freeman, R.; Berriman, J. A.; Homo, J.-C. Electron Microscopy of Frozen Water and Aqueous Solutions. *J. Microsc.* **1982**, *128* (3), 219–237. https://doi.org/10.1111/j.1365-2818.1982.tb04625.x.
(28) Mangolini, F.; Li, Z.; Marcus, M. A.; Schneider, R.; Dienwiebel, M. Quantification of the Carbon Bonding State in Amorphous Carbon Materials: A Comparison between EELS and NEXAFS Measurements. *Carbon* **2021**, *173*, 557–564. https://doi.org/10.1016/j.carbon.2020.11.021.
(29) Hitchcock, A. P.; Dynes, J. J.; Johansson, G.; Wang, J.; Botton, G. Comparison of NEXAFS Microscopy and TEM-EELS for Studies of Soft Matter. *Micron* **2008**, *39* (6), 741–748. https://doi.org/10.1016/j.micron.2007.09.010.
(30) Goode, A. E.; Porter, A. E.; Ryan, M. P.; McComb, D. W. Correlative Electron and X-Ray Microscopy: Probing Chemistry and Bonding with High Spatial Resolution. *Nanoscale* **2015**, *7* (5), 1534–1548. https://doi.org/10.1039/C4NR05922K.
(31) Cebula, I.; Lu, H.; Zharnikov, M.; Buck, M. Monolayers of Trimesic and Isophthalic Acid on Cu and Ag: The Influence of Coordination Strength on Adsorption Geometry. *Chem. Sci.* **2013**, *4* (12), 4455–4464. https://doi.org/10.1039/C3SC52137K.
(32) Okajima, T.; Teramoto, K.; Mitsumoto, R.; Oji, H.; Yamamoto, Y.; Mori, I.; Ishii, H.; Ouchi, Y.; Seki, K. Polarized NEXAFS Spectroscopic Studies of Poly(Butylene Terephthalate), Poly(Ethylene Terephthalate), and Their Model Compounds. *J. Phys. Chem. A* **1998**, *102* (36), 7093–7099. https://doi.org/10.1021/jp981164t.
(33) Varlot, K.; Martin, J. M.; Quet, C. EELS Analysis of PMMA at High Spatial Resolution. *Micron* **2001**, *32* (4), 371–378. https://doi.org/10.1016/S0968-4328(00)00017-2.
(34) Kolczewski, C.; Püttner, R.; Martins, M.; Schlachter, A. S.; Snell, G.; Sant'Anna, M. M.; Hermann, K.; Kaindl, G. Spectroscopic Analysis of Small Organic Molecules: A Comprehensive near-Edge x-Ray-Absorption Fine-Structure Study of C6-Ring-Containing Molecules. *J. Chem. Phys.* **2006**, *124* (3), 034302. https://doi.org/10.1063/1.2139674.
(35) Hitchcock, A. P.; Urquhart, S. G.; Rightor, E. G. Inner-Shell Spectroscopy of Benzaldehyde, Terephthalaldehyde, Ethylbenzoate, Terephthaloyl Chloride and Phosgene: Models for Core Excitation of Poly(Ethylene Terephthalate). *J. Phys. Chem.* **1992**, *96* (22), 8736–8750. https://doi.org/10.1021/j100201a015.
(36) Leapman, R. D.; Sun, S. Cryo-Electron Energy Loss Spectroscopy: Observations on Vitrified Hydrated Specimens and Radiation Damage. *Ultramicroscopy* **1995**, *59* (1), 71–79. https://doi.org/10.1016/0304-3991(95)00019-W.
(37) Kłosowski, M. M.; Friederichs, R. J.; Nichol, R.; Antolin, N.; Carzaniga, R.; Windl, W.; Best, S. M.; Shefelbine, S. J.; McComb, D. W.; Porter, A. E. Probing Carbonate in Bone Forming Minerals on the Nanometre Scale. *Acta Biomater.* **2015**, *20*, 129–139. https://doi.org/10.1016/j.actbio.2015.03.039.
(38) Nitiputri, K.; Ramasse, Q. M.; Autefage, H.; McGilvery, C. M.; Boonrungsiman, S.; Evans, N. D.; Stevens, M. M.; Porter, A. E. Nanoanalytical Electron Microscopy Reveals A Sequential Mineralization Process Involving Carbonate-Containing Amorphous Precursors. *ACS Nano* **2016**, *10* (7), 6826–6835. https://doi.org/10.1021/acsnano.6b02443.
(39) Kim, E.; Agarwal, S.; Kim, N.; Hage, F. S.; Leonardo, V.; Gelmi, A.; Stevens, M. M. Bioinspired Fabrication of DNA–Inorganic Hybrid Composites Using Synthetic DNA. *ACS Nano* **2019**, *13* (3), 2888–2900. https://doi.org/10.1021/acsnano.8b06492.

(40) Gay, C.; Letavernier, E.; Verpont, M.-C.; Walls, M.; Bazin, D.; Daudon, M.; Nassif, N.; Stéphan, O.; de Frutos, M. Nanoscale Analysis of Randall's Plaques by Electron Energy Loss Spectromicroscopy: Insight in Early Biomineral Formation in Human Kidney. *ACS Nano* **2020**, *14* (2), 1823–1836. https://doi.org/10.1021/acsnano.9b07664.
(41) Hidalgo, T.; Giménez-Marqués, M.; Bellido, E.; Avila, J.; Asensio, M. C.; Salles, F.; Lozano, M. V.; Guillevic, M.; Simón-Vázquez, R.; González-Fernández, A.; Serre, C.; Alonso, M. J.; Horcajada, P. Chitosan-Coated Mesoporous MIL-100(Fe) Nanoparticles as Improved Bio-Compatible Oral Nanocarriers. *Sci. Rep.* **2017**, *7* (1), 43099. https://doi.org/10.1038/srep43099.
(42) Giménez-Marqués, M.; Bellido, E.; Berthelot, T.; Simón-Yarza, T.; Hidalgo, T.; Simón-Vázquez, R.; González-Fernández, Á.; Avila, J.; Asensio, M. C.; Gref, R.; Couvreur, P.; Serre, C.; Horcajada, P. GraftFast Surface Engineering to Improve MOF Nanoparticles Furtiveness. *Small* **2018**, *14* (40), 1801900. https://doi.org/10.1002/smll.201801900.
(43) Chen, S.-Y.; Gloter, A.; Zobelli, A.; Wang, L.; Chen, C.-H.; Colliex, C. Electron Energy Loss Spectroscopy and Ab Initio Investigation of Iron Oxide Nanomaterials Grown by a Hydrothermal Process. *Phys. Rev. B* **2009**, *79* (10), 104103. https://doi.org/10.1103/PhysRevB.79.104103.
(44) Zubavichus, Y.; Shaporenko, A.; Grunze, M.; Zharnikov, M. Innershell Absorption Spectroscopy of Amino Acids at All Relevant Absorption Edges. *J. Phys. Chem. A* **2005**, *109* (32), 6998–7000. https://doi.org/10.1021/jp0535846.
(45) Babaa, M.-R.; Bantignies, J.-L.; Alvarez, L.; Parent, P.; Normand, F. L.; Gulas, M.; Mane, J. M.; Poncharal, P.; Doyle, B. P. NEXAFS Study of Multi-Walled Carbon Nanotubes Functionalization with Sulfonated Poly(Ether Ether Ketone) Chains. *J. Nanosci. Nanotechnol.* **2007**, *7* (10), 3463–3467. https://doi.org/10.1166/jnn.2007.816.
(46) Varlot, K.; Martin, J. M.; Quet, C.; Kihn, Y. Towards Sub-Nanometer Scale EELS Analysis of Polymers in the TEM. *Ultramicroscopy* **1997**, *68* (2), 123–133. https://doi.org/10.1016/S0304-3991(97)00019-3.
(47) Andrade, P. H. M. Synthesis of TiO2@MOF Composites for the Photodegradation of Organic Pollutants. Master dissertation, Universidade Federal de Minas Gerais, Brasil, 2021. https://repositorio.ufmg.br/handle/1843/38408 (accessed 2022-03-11).
(48) Shih, Y.-H.; Chien, C.-H.; Singco, B.; Hsu, C.-L.; Lin, C.-H.; Huang, H.-Y. Metal–Organic Frameworks: New Matrices for Surface-Assisted Laser Desorption–Ionization Mass Spectrometry. *Chem. Commun.* **2013**, *49* (43), 4929–4931. https://doi.org/10.1039/C3CC40934A.
(49) Nivetha, R.; Gothandapani, K.; Raghavan, V.; Jacob, G.; Sellappan, R.; Bhardwaj, P.; Pitchaimuthu, S.; Kannan, A. N. M.; Jeong, S. K.; Grace, A. N. Highly Porous MIL-100(Fe) for the Hydrogen Evolution Reaction (HER) in Acidic and Basic Media. *ACS Omega* **2020**, *5* (30), 18941–18949. https://doi.org/10.1021/acsomega.0c02171.
(50) Scott, A. I. *Interpretation of the Ultraviolet Spectra of Natural Products: International Series of Monographs on Organic Chemistry*; Elsevier, 2013.
(51) Subudhi, S.; Mansingh, S.; Swain, G.; Behera, A.; Rath, D.; Parida, K. HPW-Anchored UiO-66 Metal–Organic Framework: A Promising Photocatalyst Effective toward Tetracycline Hydrochloride Degradation and H2 Evolution via Z-Scheme Charge Dynamics. *Inorg. Chem.* **2019**, *58* (8), 4921–4934. https://doi.org/10.1021/acs.inorgchem.8b03544.
(52) Man, Z.; Meng, Y.; Lin, X.; Dai, X.; Wang, L.; Liu, D. Assembling UiO-66@TiO2 Nanocomposites for Efficient Photocatalytic Degradation of Dimethyl Sulfide. *Chem. Eng. J.* **2022**, *431*, 133952. https://doi.org/10.1016/j.cej.2021.133952.

(53) Leloire, M.; Walshe, C.; Devaux, P.; Giovine, R.; Duval, S.; Bousquet, T.; Chibani, S.; Paul, J.-F.; Moissette, A.; Vezin, H.; Nerisson, P.; Cantrel, L.; Volkringer, C.; Loiseau, T. Capture of Gaseous Iodine in Isoreticular Zirconium-Based UiO-n Metal-Organic Frameworks: Influence of Amino Functionalization, DFT Calculations, Raman and EPR Spectroscopic Investigation. *Chem. – Eur. J.* **2022**, *28* (14), e202104437. https://doi.org/10.1002/chem.202104437.
(54) Ritsko, J. J.; Brillson, L. J.; Bigelow, R. W.; Fabish, T. J. Electron Energy Loss Spectroscopy and the Optical Properties of Polymethylmethacrylate from 1 to 300 EV. *J. Chem. Phys.* **1978**, *69* (9), 3931–3939. https://doi.org/10.1063/1.437131.
(55) Vinu, R.; Madras, G. Photocatalytic Degradation of Methyl Methacrylate Copolymers. *Polym. Degrad. Stab.* **2008**, *93* (8), 1440–1449. https://doi.org/10.1016/j.polymdegradstab.2008.05.018.
(56) Yakovlev, S.; Libera, M. Dose-Limited Spectroscopic Imaging of Soft Materials by Low-Loss EELS in the Scanning Transmission Electron Microscope. *Micron* **2008**, *39* (6), 734–740. https://doi.org/10.1016/j.micron.2007.10.019.
(57) Schneider, N. M.; Norton, M. M.; Mendel, B. J.; Grogan, J. M.; Ross, F. M.; Bau, H. H. Electron–Water Interactions and Implications for Liquid Cell Electron Microscopy. *J. Phys. Chem. C* **2014**, *118* (38), 22373–22382. https://doi.org/10.1021/jp507400n.
(58) Sousa, A.; Aitouchen, A.; Libera, M. Water Mapping in Hydrated Soft Materials. *Ultramicroscopy* **2006**, *106* (2), 130–145. https://doi.org/10.1016/j.ultramic.2005.06.059.
(59) Leclerc, H.; Vimont, A.; Lavalley, J.-C.; Daturi, M.; Wiersum, A. D.; Llwellyn, P. L.; Horcajada, P.; Férey, G.; Serre, C. Infrared Study of the Influence of Reducible Iron(III) Metal Sites on the Adsorption of CO, CO2, Propane, Propene and Propyne in the Mesoporous Metal–Organic Framework MIL-100. *Phys. Chem. Chem. Phys.* **2011**, *13* (24), 11748–11756. https://doi.org/10.1039/C1CP20502A.
(60) Horcajada, P.; Surblé, S.; Serre, C.; Hong, D.-Y.; Seo, Y.-K.; Chang, J.-S.; Grenèche, J.-M.; Margiolaki, I.; Férey, G. Synthesis and Catalytic Properties of MIL-100(Fe), an Iron(Iii) Carboxylate with Large Pores. *Chem. Commun.* **2007**, *0* (27), 2820–2822. https://doi.org/10.1039/B704325B.
(61) March, K.; Venkatraman, K.; Truong, C. D.; Williams, D.; Chiu, P.-L.; Rez, P. Protein Secondary Structure Signatures from Energy Loss Spectra Recorded in the Electron Microscope. *J. Microsc.* **2021**, *282* (3), 215–223. https://doi.org/10.1111/jmi.12995.
(62) Jokisaari, J. R.; Hachtel, J. A.; Hu, X.; Mukherjee, A.; Wang, C.; Konecna, A.; Lovejoy, T. C.; Dellby, N.; Aizpurua, J.; Krivanek, O. L.; Idrobo, J.-C.; Klie, R. F. Vibrational Spectroscopy of Water with High Spatial Resolution. *Adv. Mater.* **2018**, *30* (36), 1802702. https://doi.org/10.1002/adma.201802702.
(63) Li, X.; Haberfehlner, G.; Hohenester, U.; Stéphan, O.; Kothleitner, G.; Kociak, M. Three-Dimensional Vectorial Imaging of Surface Phonon Polaritons. *Science* **2021**, *371* (6536), 1364–1367. https://doi.org/10.1126/science.abg0330.
(64) Rodil, S. E. Infrared Spectra of Amorphous Carbon Based Materials. *Diam. Relat. Mater.* **2005**, *14* (8), 1262–1269. https://doi.org/10.1016/j.diamond.2005.01.044.
(65) Agostoni, V.; Horcajada, P.; Noiray, M.; Malanga, M.; Aykaç, A.; Jicsinszky, L.; Vargas-Berenguel, A.; Semiramoth, N.; Daoud-Mahammed, S.; Nicolas, V.; Martineau, C.; Taulelle, F.; Vigneron, J.; Etcheberry, A.; Serre, C.; Gref, R. A "Green" Strategy to Construct Non-Covalent, Stable and Bioactive Coatings on Porous MOF Nanoparticles. *Sci. Rep.* **2015**, *5* (1), 7925. https://doi.org/10.1038/srep07925.

For Table of Contents Only